RSC Advances

PAPER

Cite this: *RSC Adv.*, 2015, **5**, 79845

High performance of MoS_2 microflowers with a water-based binder as an anode for Na-ion batteries†

P. Ramesh Kumar, Young Hwa Jung and Do Kyung Kim*

Received 13th August 2015
Accepted 14th September 2015

DOI: 10.1039/c5ra16297a

www.rsc.org/advances

Na-ion batteries have risen as an alternative system to current Li-ion batteries due to the wide range of availability and low price of sodium resources. Here we report the binder effect on sodium storage properties of MoS_2 microflowers with nano-sized petals which are prepared by a combination of a hydrothermal reaction and solid-state reaction. The electrochemical performance of MoS_2 microflowers with different binders is evaluated against pure Na metal in a half-cell configuration through a conversion reaction. Especially, the electrode of MoS_2 microflowers with a Na-alginate binder shows an excellent cycling stability, delivering a high discharge capacity of 595 mA h g^{-1} after 50 cycles. The MoS_2 microflowers with the Na-alginate binder also exhibit high rate capability, retaining a capacity of 236 mA h g^{-1} at 10C without any carbonaceous materials. The improved electrochemical performance was mainly attributed to the synergetic effect of the morphology of the MoS_2 microflowers and good adhesive capabilities of the alginate binder. Furthermore, we report a Na-ion fuel cell using the MoS_2 microflower anode with $Na_3V_2O_{2x}(PO_4)_2F_{3-2x}$/C as a cathode material.

1. Introduction

Na-ion batteries have been a focus recently since sodium is very cheap and abundant on the earth's crust, which makes it the most advantageous element for battery applications after lithium.[1–4] Compared to Li-ion batteries, Na-ion batteries still have many obstacles for commercialization, although researchers have proposed a number of electrode materials for Na-ion batteries.[5–7] In particular, the negative electrode for Na-ion batteries is one of the major challenging issues, because graphite, the representative anode material for Li-ion batteries, shows low Na-ion intercalation/deintercalation capability.[8] Pure Na metal also cannot be used because of dendrite formation while charging–discharging and low melting point which causes safety issues. Hence, researchers have proposed several new anode candidates such as $Na_2Ti_3O_7$, Sb_2O_4, TiO_2, $Na_2C_8H_4O_4$, and SnSb/C for Na-ion batteries.[9–13]

Compared to other existing anode materials, metal sulfides possess high theoretical specific capacities and comparatively low cost. Molybdenum disulfide (MoS_2) is a promising material which has the dichalcogenide structure, with the molybdenum atoms coordinated by six sulfur atoms.[14] Most of all, the laminar MoS_2 bonded through weak van der Waals forces can host metal cations.[15] Thus, MoS_2 has been studied as an intercalation host for lithium.[16,17] Very large number of works on Li/MoS_2 has been done, but very few papers were demonstrated as Na interaction host for Na-ion batteries. Park *et al.* presented the electrochemical behaviours of Na/MoS_2 cells at each discharge depth through analysis of the crystallographic changes by employing *ex situ* X-ray diffraction (XRD) and transmission electron microscopy (TEM).[18] David *et al.* showed that the MoS_2/graphene composite paper delivered good Na cycling ability with a stable charge capacity of ~230 mA h g^{-1} with 99% efficiency.[19] Wang *et al.* reported MoS_2/C nanospheres as a promising anode for high performance sodium-ion batteries due to high specific capacity (520 mA h g^{-1} at 0.1C).[20] Xie *et al.* prepared MoS_2/graphene composite by hydrothermal method as an anode material for Na-ion batteries. And they tried to understand the synergistic effect between layered sulfides and graphene using computational studies.[21] some researchers have presented high-performance MoS_2/graphene composites for Na-ion batteries and Na-ion pseudo-capacitors by different methods.[22,23] Recently, Bang *et al.* demonstrated stable operation of a Na-ion battery by using the exfoliated MoS_2 nanosheets as an intercalation anode with stable discharge capacity of 160 mA h g^{-1}.[24]

In this work, we present the high capacity pure MoS_2 microflowers with nanopetals as an attractive candidate for Na-ion battery negative electrode material. We have combined MoS_2 microflowers with different binders to improve the interface between active materials and the current collector. MoS_2 microflowers were prepared by using hydrothermal followed by calcination to obtain pure microflowers. The electrochemical response of the prepared nanoparticles was studied

Department of Materials Science and Engineering, Korea Advanced Institute of Science and Technology (KAIST), Daejeon 305-701, Republic of Korea. E-mail: dkkim@kaist.ac.kr

† Electronic supplementary information (ESI) available: An equivalent circuit, XRD, SEM and CV of $Na_3V_2O_{2x}(PO_4)_2F_{3-2x}$ sample. See DOI: 10.1039/c5ra16297a

using cyclic voltammetry and galvanostatic charge–discharge measurements. These MoS_2 microflowers with sodium alginate binder could exhibit promising electrochemical performance such as high reversible capacity, excellent cycling performance and good rate capability when compared to other binders like polyvinylidene fluoride (PVDF) and polyethylene oxide (PEO).

2. Experimental

2.1 Synthesis of MoS_2 microflowers

First of all, $(NH_4)_2MoS_4$ was prepared by a procedure similar to that previously reported.[25] H_2S was passed through the solution of ammonium hydroxide and ammonium hepta-molybdenum. The temperature rise to 60 °C, and H_2S bubbling was stopped as soon as the reaction mixture colored was turn in to pink. The pink colour $(NH_4)_2MoS_4$ solution was transferred to a 80 mL Teflon-lined autoclave and placed inside a muffle furnace at 180 °C for 24 h. Black precipitates were obtained after the hydrothermal treatment, filtered, washed with deionized water, and dried at 80 °C for 12 h. The final pure MoS_2 powders were prepared by calcination at 700 °C for 4 h in argon atmosphere.

2.2 Preparation of $Na_3V_2O_{2x}(PO_4)_2F_{3-2x}$/C cathode material

To prepare the $Na_3V_2O_{2x}(PO_4)_2F_{3-2x}$/C composite by hydrothermal reaction, the precursor, $[V(PO_3)_3]_n$/C composite, is firstly prepared by the solid-state reaction with stoichiometric amounts of V_2O_5, $NH_4H_2PO_4$, and super P carbon. This mixture was annealed twice under N_2 atmosphere at 300 and 850 °C. After that, $Na_3V_2O_{2x}(PO_4)_2F_{3-2x}$/C composite was prepared under hydrothermal conditions by reacting NaF and $[V(PO_3)_3]_n$/C in a 3.3 : 1 molar ratio. The reaction mixture was sealed in a polytetrafluoroethylene (PTFE)-lined steel pressure vessel, which was maintained at 170 °C for 72 h. This carbon content of precursor material prevents the complete oxidation from V^{3+} to V^{4+} in presence of water. Then the product was dried at 80 °C for 12 h in an electric oven.

2.3 Characterization

Structural characterization of the materials was performed by the powder X-ray diffraction (XRD) employing Cu-Kα (1.54 Å) radiation (RIGAKU, D/MAX-2500 powder X-ray diffractometer). Particle size and morphology analysis were characterized employing a field emission scanning electron microscope (FE-SEM Hitachi S-4800, Japan) and a transmission electron microscope with energy dispersive spectroscopy (TEM), JEOL 2010F HRTEM, Japan, with a 300 kV operating voltage. The Raman spectra of powders were recorded at room temperature employing a HR 800 Raman spectrophotometer (Jobin Yvon-Horiba, France) using monochromatic He–Ne LASER (633 nm), operating at 20 mW.

2.4 Electrochemical measurements

The electrochemical studies of the synthesized MoS_2 flowers were analyzed in CR2032 coin cells. The composite electrode was prepared by mixing 80 wt% of active material with 10 wt% of super P carbon and 10 wt% of PVDF, PEO and sodium alginate binders in suitable solvent. The obtained slurry was coated on a piece of Cu foil and cut into 12 mm diameter circular electrodes. Sodium metal was used as an anode and 1 M $NaClO_4$ in propylene carbonate (PC) with 2 vol% fluoroethylene carbonate (FEC) was used as electrolytes. CR2032 cells were assembled in an argon-filled dry glove box (M.O. Tech, South Korea) using Whatman GF/D borosilicate glass-fibre separator. The cyclic voltammetry and *ex situ* electrochemical impedance spectroscopy at various potentials during first discharge–charge cycle were measured using Biologic Science Instruments (Model: VMP3) between 1 MHz and 2 mHz under AC stimuli with 5 mV of amplitude. The cells were galvanostatically cycled (WBCS3000, Automatic battery cycler system, Wonatech, South Korea) between 3 V and 0.002 V. The $Na_3V_2O_{2x}(PO_4)_2F_{3-2x}$/C composite was used as a cathode material in testing Na-ion full cells. The detailed procedure to make a full-cell is described in our previous paper.[26] The mass loading for the cathode and the anode is 2.2 mg and 2.8 mg, respectively, and the area for the cathode and the anode is 1.13 cm^2 and 1.54 cm^2, respectively. The $MoS_2/Na_3V_2O_{2x}(PO_4)_2F_{3-2x}$ full-cell was galvanostatically tested within the voltage of 1.0 and 3.0 V at 25 °C. All gravimetric capacity was calculated by the weight of the cathode.

3. Results and discussion

3.1 Structural analysis

Fig. 1a shows the XRD patterns of the MoS_2 microflowers which are indexed with hexagonal structure with the space group $P6_3/mmc$ (JCPDS #37-1492). Raman spectrum for the pure MoS_2

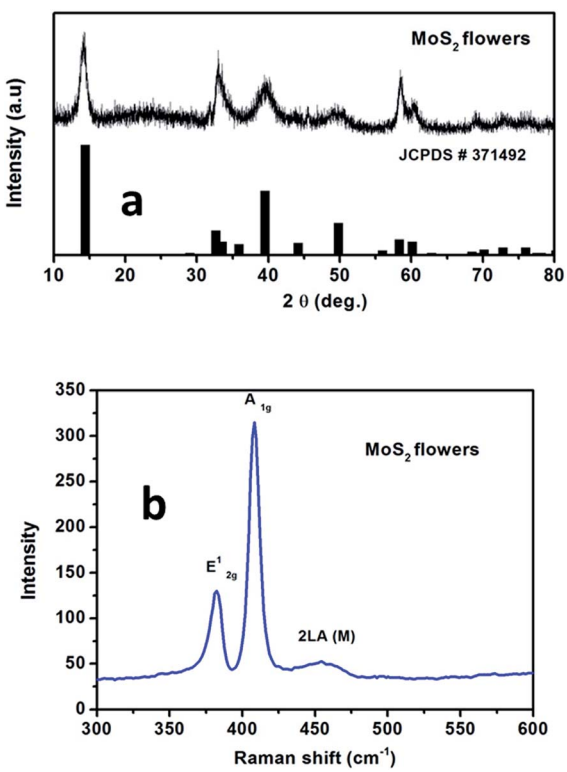

Fig. 1 (a) XRD patterns and (b) Raman spectrum for the MoS_2 microflowers.

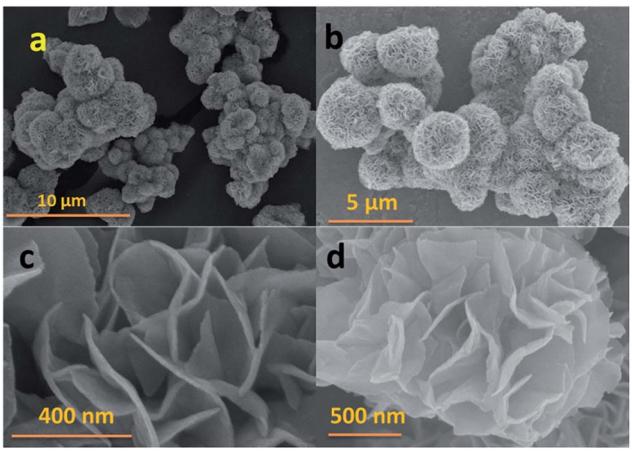

Fig. 2 SEM images of prepared MoS_2 microflowers with nano-sized petals in different magnifications (a–d).

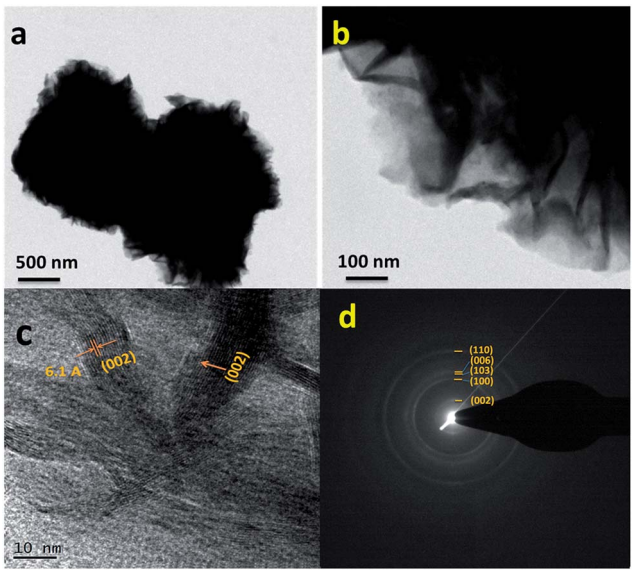

Fig. 3 (a and b) TEM images in different magnifications, (c) high resolution image, and (d) SAED patterns for the MoS_2 microflowers.

microflowers is shown in Fig. 1b. The peaks at 385.6 cm^{-1} (E^1_{2g}) and 408 cm^{-1} (A^1_g) are originated from the vibration of Mo–S in-plane and out-of-plane vibration modes respectively. Furthermore, the peak at around 454 cm^{-1} (2LA) is observed due to the resonance Raman (RR) scattering while using 633 nm laser source.[27,28] Hence, it is confirmed that the prepared sample is in pure single phase. The microstructure of as-prepared MoS_2 microflowers was obtained from both SEM and TEM micrographs. Fig. 2 shows the SEM images for pure MoS_2 microflowers in different magnifications. The size of typical microflowers is approximately 3 μm in width. TEM images of prepared MoS_2 microflowers samples were shown in Fig. 3. The HRTEM image of the MoS_2 microflowers (Fig. 3c) indicates the formation of flowers with petal morphology of ~10 nm in thickness. From Fig. 3d, the observed Debye–Scherrer rings represent the (002), (100), (103), (006) and (110) lattice planes and confirm the phase and purity of MoS_2 microflowers.

3.2 Electrochemical activities

Fig. 4 presents cyclic voltammetry (CV) plots of MoS_2 microflowers with PVDF, PEO, heat treated PVDF (*i.e.* electrode prepared by PVDF and heated at 250 °C for 3 h), and Na-alginate binders, respectively. In the first scan, three cathodic peaks were observed at 0.8, 0.65, and 0.15 V for MoS_2 with PVDF and PEO, the first two peaks at 0.8 V and 0.65 V belong with the sodium intercalation into the MoS_2 structure and the third peak at 0.15 V corresponds to the conversion reactions of Na^+ and Mo^{4+} to their metallic state along with the formation of Na_2S.[18] The broad anodic peak at around 1.8 V for two samples (PVDF and PEO) can be ascribed to the oxidation reactions of metallic Mo, which is corresponding to oxidation at 2.2 V in lithium ion batteries.[29] From Fig. 4, the cathodic peaks of MoS_2 with PVDF and PEO binder are shifting to higher potentials with reducing their intensities from the second scan onwards, which is indicating that lower electrochemical stabilities of these materials. In case of electrodes with both heated PVDF and Na-alginate, they show only one redox peak at 0.35 V and 0.65 V, respectively.

In Fig. 4c and d, the broad anodic peaks observed between 1.6 and 2.1 V correspond to the reduction of S to Na_2S from the second cycle. Other anodic peaks at 0.8 V and 0.1 V are attributed to the association of Na with Mo. Among the three cathodic peaks, the peaks at 0.5 and 1.65 V represent the oxidation of Mo and the peak at 2.3 V is due to the conversion from element S_8 to polysulfide and then to Na_2S.[30] The peak intensity is stable for the MoS_2 microflowers with PVDF heat-treated electrode and Na-alginate binder, still the PVDF heat-treated electrode has small noise due to the formation of very small oxide whiskers on copper foil surface at 250 °C.[31] Hence, these cyclic voltammetry results indicate that MoS_2 microflowers with alginate binder exhibits better electrochemical properties than other binders due to the high surface interaction between microflowers and Na-alginate binder.[32,33]

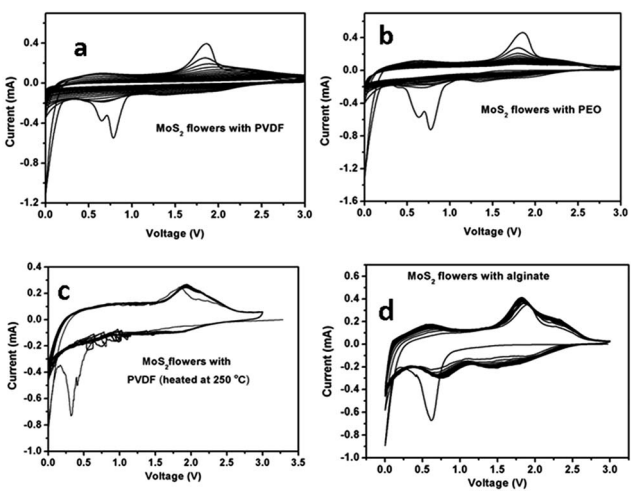

Fig. 4 Cyclic voltammetry plots for MoS_2 microflowers with (a) PVDF, (b) PEO, (c) PVDF heated electrode at 250 °C and (d) Na-alginate.

The mechanism of the conversion reaction of MoS_2 microflowers with sodium is different with the insertion/deinsertion of sodium into host structures reactions. The reversible electrochemical reaction mechanism of Na with the metal sulfides is as follows.

$$MoS_2 + 2Na^+ + 2e^- \leftrightarrow Na_2MoS_2 \quad (1)$$

$$Na_2MoS_2 + 2Na^+ + 2e^- \leftrightarrow Mo + 2Na_2S \quad (2)$$

The cycling performances of MoS_2 microflowers with different binders are shown in Fig. 5. Fig. 5a exhibits the cyclic stability plots for MoS_2 microflowers with PVDF, heated-PVDF, PEO, and Na-alginate binder, respectively. The MoS_2 microflowers with Na-alginate and PVDF heat-treated at 250 °C electrode show the higher cyclic stability than the electrodes using conventional PVDF and PEO as binders. Even, Na-alginate binder is showing better stability compared to the PVDF heat-treated electrode after 50 cycles. MoS_2 microflowers with all binders were cycled at 0.1C rate (67 mA g^{-1}). By using PVDF as binder, MoS_2 microflowers deliver an initial discharge capacity of 680 mA h g^{-1}, but later on, it shows a negligible discharge capacity of 9 mA h g^{-1} with high capacity fading after 50 cycles. Fig. 5c shows the charge–discharge curves of MoS_2 microflowers with PVDF binder up to 50 cycles. MoS_2 microflowers with PVDF binder heat-treated at 250 °C for 3 h deliver the first discharge capacity of 1065 mA h g^{-1} which is higher than its theoretical capacity. At first discharge, MoS_2 microflowers might play a role as an electrochemical catalyst for the reversible conversion of some solid electrolyte interface components thereby it could contribute on additional discharge capacity.[34] After that, a reversible capacity of 495 mA h g^{-1} was maintained after 50 cycles with 98% coulombic efficiency (Fig. 5d), revealing its high cycle stability nature as previously reported with Fe_3O_4 conversion anodes.[35] While MoS_2 microflowers with PEO binder deliver an initial discharge capacity of 650 mA h g^{-1}, but the discharge capacity is significantly decreased to 44 mA h g^{-1} after 30 cycles (Fig. 5e). The charge–discharge profile for the MoS_2 microflowers with Na-alginate binder for 50 cycles is represented in Fig. 5f. The MoS_2 microflowers with Na-alginate binder deliver an initial discharge capacity of 820 mA h g^{-1} and retain 595 mA h g^{-1} after 50 cycles with 99% coulombic efficiency, indicating its excellent cycle stability.

The MoS_2 microflowers with Na-alginate binder exhibit the considerable performance even at high current rates. The discharge capacities of the MoS_2 microflowers with Na-alginate binder at a current of 670 mA g^{-1} (1C), 1340 mA g^{-1} (2C), 3350 mA g^{-1} (5C) and 6700 mA g^{-1} (10C) for 10 cycles, respectively, are shown in Fig. 6. Without any carbonaceous materials, the MoS_2 microflowers with Na alginate binder deliver a stable discharge capacity of 240 mA g^{-1} at high current rate of 6700 mA g^{-1} (10C). It is noted that nearly the same capacity can be

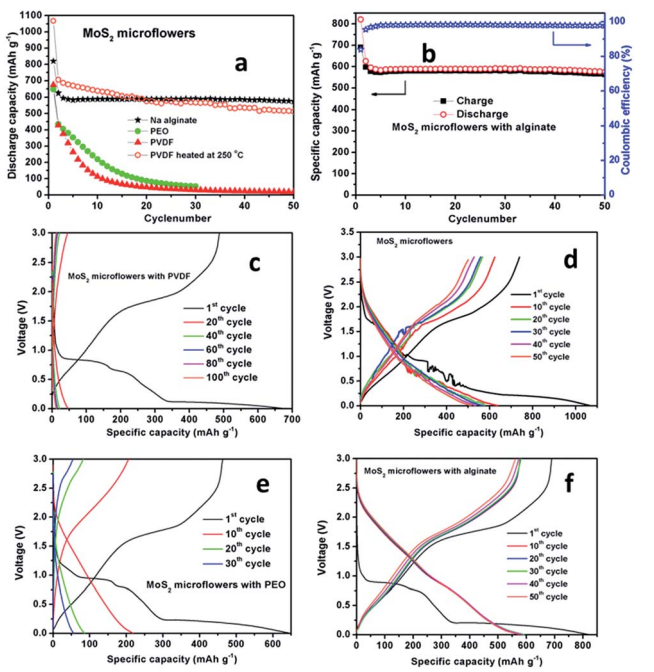

Fig. 5 (a) Cyclability of MoS_2 microflowers with different binders. (b) Capacity retention and coulombic efficiency of MoS_2 microflowers with Na-alginate binder. Charge–discharge curves for the MoS_2 microflowers with (c) PVDF binder, (d) PVDF binder heated up to 250 °C for 3 h, (e) PEO binder, and (f) Na-alginate binder.

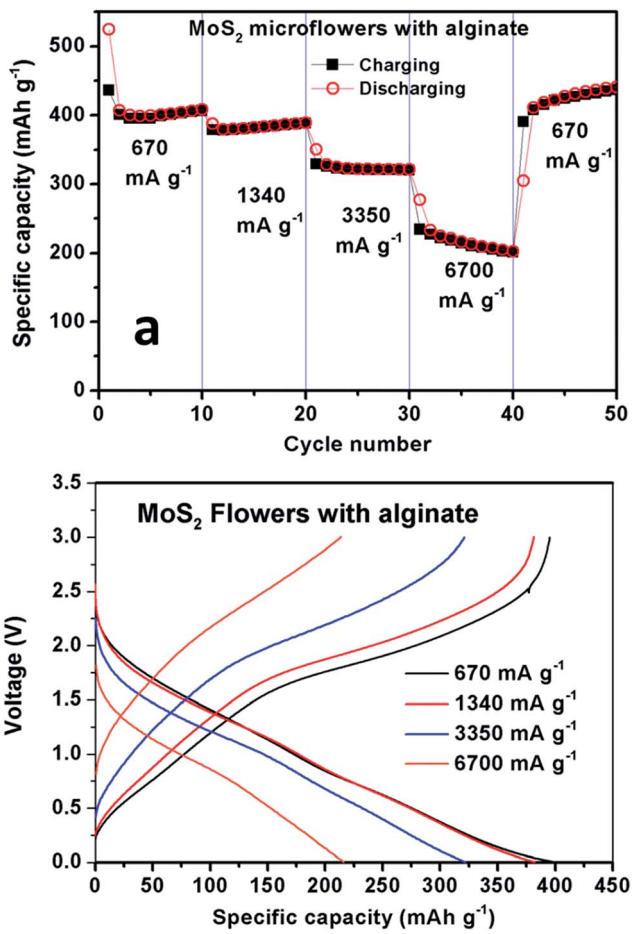

Fig. 6 (a) Rate capability and (b) charge–discharge voltage curves at different current rates for the MoS_2 microflowers with Na-alginate binder.

regained for the electrode when the current density is turned back to 670 mA g^{-1} and the plateau region in all discharge curves can be observed at high current rates, indicating superior stability of the MoS_2 microflowers/alginate anode. Again, the enhancement of electrochemical performances in MoS_2 microflowers/alginate anode might be attributed to the strong bonding between active materials and carboxyl groups on binder surface during cycling.[32]

In order to understand the electrochemical behavior of the MoS_2 microflowers with alginate binder during cycling, electrochemical impedance spectroscopy (EIS) measurements were carried out during first cycle at different voltages, as shown in Fig. 7.

The scatters in Fig. 7 represent the experimental data points and the solid lines represent the fitted data in the Nyquist plots for the MoS_2 microflowers/alginate. The latter were analyzed by fitting with an electrical equivalent circuit consisting of resistors and constant phase elements displayed in Fig. S1.† The electrical equivalent circuit elements are electrolyte resistance (R_e), the separable surface film (SF) and charge transfer (CT) impedances R_{SF} and R_{CT}, also constant phase elements CPE_{SF} and CPE_{CT} and the finite Warburg impedance (W_d). The depressed semi-circles in the spectra were represented by parallel combination of constant phase elements (CPE's) and resistance. The experimental data was fitted by using *Z-fit* software with fitting except at low frequencies.

In Fig. 7a, the MoS_2 microflowers/alginate impedance results showed that the electrolyte resistance (R_e) remained almost constant at 5.4 Ω irrespective of voltage while discharging or charging. Two semi-circles were observed in high and middle frequency range from Fig. 7a. The first semicircle at higher frequency is related to the formation of passivation film on the surface (SF) and the charge transfer process at interface (CT). The second semicircle at low frequency is related to electronic properties of the materials, which is represented as bulk. The Nyquist plot of the cell at OCV consists of a depressed semi-circle followed by Warburg element at low frequencies. This is attributed to the surface film impedance and the values as per fitting are shown in Table S1.† At OCV, only surface film will contribute to the resistance, and it depends on concentration of electrolytes. In addition, solid electrolyte interphase (SEI) formation/partial dissolution/re-formation also takes place on cycling. This is reflected in the changes in the value of surface film impedance (R_{SF}) up on cycling.[36,37]

Also at 2 V, the impedance plot consists similar to that at OCV. At 1.6 V and 0.8 V, the Nyquist plots contain two semi-circles in the high and intermediate frequency range and a sloping line in the low-frequency region. This is exactly matched with the observed CV data which indicate that the earlier stage of conversion reaction and metal nano-particle formation take place at ~1.2 V. Further discharging to 0.4 and 0.002 V, the size of first semi-circle is remained same, but size of the second

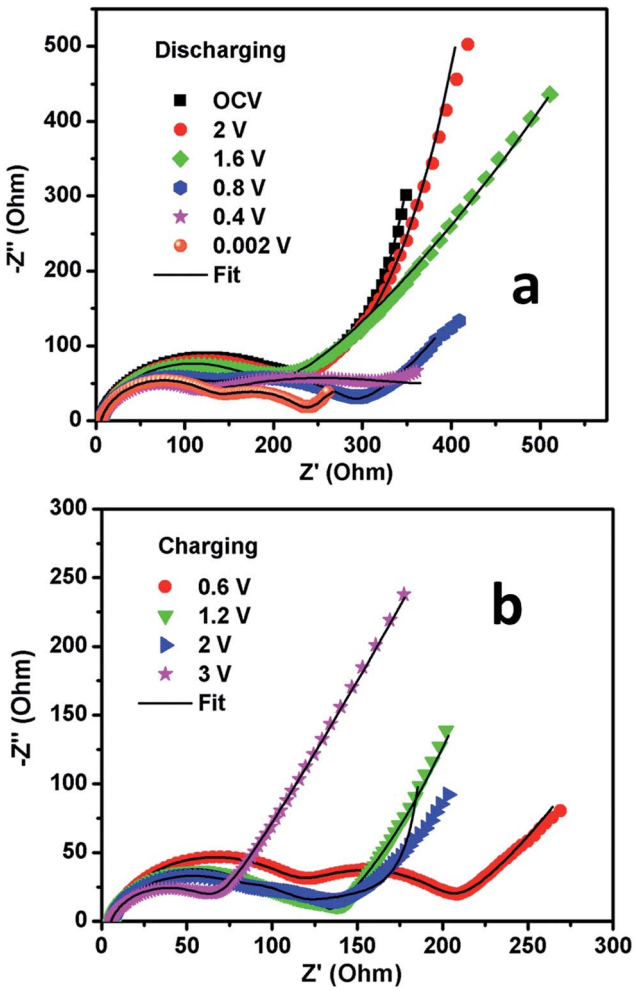

Fig. 7 Nyquist plots for the MoS_2 microflowers with Na-alginate binder electrode *vs.* Na/Na^+ while (a) discharging and (b) charging states.

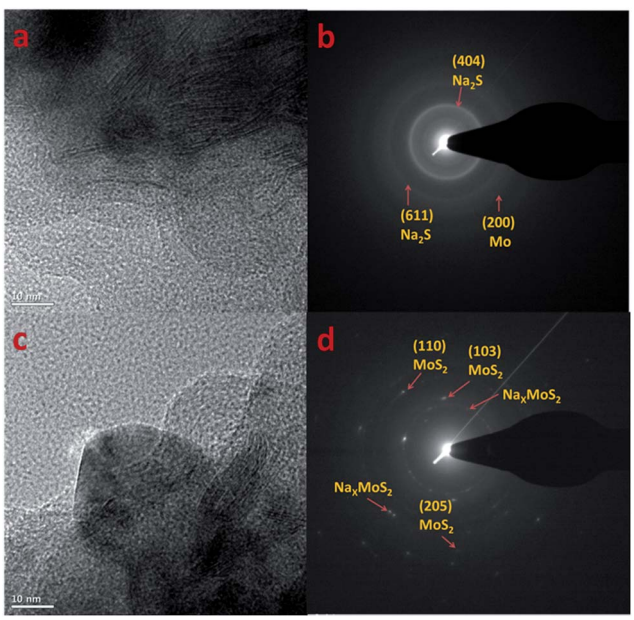

Fig. 8 (a) TEM image and (b) SAED patterns for the MoS_2 microflowers with Na-alginate binder after first discharge. (c) TEM image and (d) SAED patterns for the MoS_2 microflowers with Na-alginate binder after first charge.

semicircle is reduced which might be due to the conversion reaction.

The Nyquist plots of MoS_2/alginate anode during first charging state are shown in Fig. 7b. The impedance plots are not following same trend like first discharge, since the mechanism of first-discharge reaction is different from first-charge reaction. At 0.6 V and 1.2 V, the Nyquist plots contain high frequency semicircle along with low frequency depressed semicircle which is due to the formation of the metal oxides from the Mo metal-particles through the conversion reaction. Further charging up to 2.0 V and 3 V, the surface film and charge transfer impedance decreases ascribed to partial dissolution of polymeric gel-type layer. Hence, we concluded that the electrochemical impedance studies can support the observed CV results as well as conversion reaction mechanism.

To find the nature of the conversion reaction in the MoS_2 microflowers, *ex situ* TEM analysis were performed on the MoS_2 microflowers/alginate electrode at discharging and charging states. The *ex situ* TEM image and SAED patterns are represented in Fig. 8. The petal morphology is retained after first discharge (Fig. 8a), which indicates the high strong interaction between alginate binder and active materials. The SAED patterns in Fig. 8b shows the inter-planer distance of Mo and Na_2S at discharged state. The obtained inter-planer distance values are matched with the Miller indices of pure Mo and Na_2S. The *ex situ* TEM results for the fully charged MoS_2 microflowers/alginate electrode are shown in Fig. 8c and d. It is clear that the formation of MoS_2 and Na_xMoS_2 at charged state. Hence, it is proved that the Mo metal and sulfides formed at discharged state and the reformation of MoS_2 at charged state.

3.3 $Na_3V_2O_{2x}(PO_4)_2F_{3-2x}$/$MoS_2$ full cell

We have previously studied the feasibility of the Na-ion full cells by combining a negative electrode material, Fe_3O_4, and a positive electrode material, $Na_3V_2(PO_4)_3$.[24] However, the reversible capacity of Fe_3O_4 was quite low (~250 mA h g^{-1}), and the battery performance of the Fe_3O_4/$Na_3V_2(PO_4)_3$ full-cell should be enhanced for cyclic stability. Therefore, we assembled the coin-type full-cell consisting of the MoS_2 microflowers anode and the $Na_3V_2O_{2x}(PO_4)_2F_{3-2x}$/C composite cathode. The XRD patterns, SEM image, and electrochemical performances of the $Na_3V_2O_{2x}(PO_4)_2F_{3-2x}$/C composite are summarized in Fig. S2.† Fig. 9a shows the reversible capacity and coulombic efficiency of the MoS_2 microflowers/$Na_3V_2O_{2x}(PO_4)_2F_{3-2x}$/C full-cell at a rate of 0.1C (1C corresponds to 130 mA g^{-1}, the theoretical capacity of the $Na_3V_2O_{2x}(PO_4)_2F_{3-2x}$) in a voltage range of 1.0 and 3.0 V. The capacity retention after 40 cycles was *ca.* 72% (76 mA h g^{-1}), and the average coulombic efficiency was 96%. Fig. 9b shows the voltage profile of the full cell by 40 cycles, indicating an average operating voltage of 1.8 V. The two distinctive voltage plateaus are attributed to the $Na_3V_2O_{2x}(PO_4)_2F_{3-2x}$/C cathode, and the sloppy voltage profiles of MoS_2 anode could influence the overall voltage curve of the full-cell.

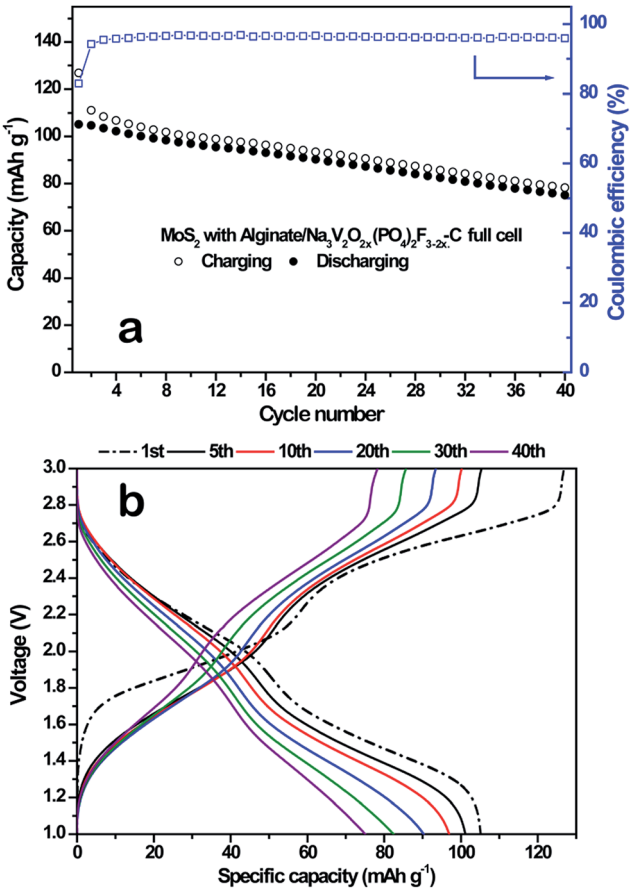

Fig. 9 (a) Cyclability and (b) charge–discharge curves for the MoS_2 micro flowers with Na-alginate binder/$Na_3V_2O_{2x}(PO_4)_2F_{3-2x}$/C full cell.

4. Conclusions

MoS_2 microflowers were prepared by hydrothermal reaction combined with solid state reaction. The prepared MoS_2 microflowers were characterized and confirmed the purity of the phase, crystallinity, microstructure and morphology information by XRD, SEM, Raman and HRTEM. Electrochemical properties of MoS_2 microflowers with different binders were investigated by using cyclic voltammetry and charge–discharge galvanostatic cycling. While MoS_2 microflowers show a high capacity fading with PVDF and PEO binder, it is shown that high capacity was retained for MoS_2 with Na-alginate binder. Furthermore, MoS_2 microflowers with Na-alginate binder offer good charge transfer kinetics due to the unbreakable electron transport network. MoS_2 microflowers/alginate electrodes shows a stable capacity of 595 mA h g^{-1} at 0.1C (67 mA g^{-1}) rate after 50 cycles. The better performance of MoS_2 microflowers/alginate can be ascribed to the stability of the interfaces providing the stable capacity retention in long-term cycling.

Acknowledgements

This work was supported by the Program to Solve Climate Changes (NRF-2010-C1AAA001-2010-0029031) of Korea (NRF) funded by the Ministry of Science, ICT & Future Planning. It was also supported by the Climate Change Research Hub of KAIST (Grant No. N01150034).

References

1 B. L. Ellis and L. F Nazar, *Curr. Opin. Solid State Mater. Sci.*, 2012, **16**, 168–177.
2 V. Palomares, P. Serras, I. Villaluenga, K. B. Hueso, J. Carretero-González and T. Rojo, *Energy Environ. Sci.*, 2012, **5**, 5884–5901.
3 S. Y. Hong, Y. Kim, Y. Park, A. Choi, N.-S. Choi and K. T. Lee, *Energy Environ. Sci.*, 2013, **6**, 2067–2081.
4 V. L. Chevrier and G. Ceder, *J. Electrochem. Soc.*, 2011, **158**, 1011–1014.
5 L. Xao, Y. Cao and J. Liu, Low-cost Nanomaterials, *Green Energy and Technology*, Springer-Verlag, London, 2014, pp. 395–424.
6 C. Masquelier and L. Croguennec, *Chem. Rev.*, 2013, **113**, 6552–65915.
7 V. Palomares, M. Casas-Cabanas, E. Castillo-Martínez, M. H. Han and T. Rojo, *Energy Environ. Sci.*, 2013, **6**, 2312–2337.
8 H. Kim, J. Hong, Y. U. Park, J. Kim, I. Hwang and K. Kang, *Adv. Funct. Mater.*, 2015, **25**, 534–541.
9 P. Senguttuvan, G. Rousse, V. Seznec, J. M. Tarascon and M. R. Palacin, *Chem. Mater.*, 2011, **23**, 4109–4111.
10 Q. Sun, Q. Q. Ren, H. Li and Z. W. Fu, *Electrochem. Commun.*, 2011, **13**, 1462–1464.
11 H. Xiong, M. D. Slater, M. Balasubramanian, C. S. Johnson and T. Rajh, *J. Phys. Chem. Lett.*, 2011, **2**, 2560–2565.
12 L. Zhao, J. Zhao, Y. S. Hu, H. Li, Z. Zhou, M. Armand and L. Chen, *Adv. Energy Mater.*, 2012, **2**, 962–965.
13 L. Xiao, Y. Cao, J. Xiao, W. Wang, L. Kovarik, Z. Nie and J. Liu, *Chem. Commun.*, 2012, **48**, 3321–3323.
14 B. G. Silbernagel, *Solid State Commun.*, 1975, **17**, 361–366.
15 E. Benavente, M. A. Santa Ana, F. Mendizábal and G. González, *Coord. Chem. Rev.*, 2002, **224**, 87–109.
16 Y. Miki, D. Nakazato, H. Ikuta, T. Uchida and M. Wakihara, *J. Power Sources*, 1995, **54**, 508–510.
17 U. K. Sen and S. Mitra, *ACS Appl. Mater. Interfaces*, 2013, **5**, 1240–1247.
18 J. Park, J. S. Kim, J. W. Park, T. H. Nam, K. W. Kim, J. H. Ahn, G. Wang and H. J. Ahn, *Electrochim. Acta*, 2013, **92**, 427–432.
19 L. David, R. Bhandavat and G. Singh, *ACS Nano*, 2014, **8**, 1759–1770.
20 J. Wang, C. Luo, T. Gao, A. Langrock, A. C. Mignerey and C. Wang, *Small*, 2015, **11**, 473–481.
21 X. Xie, Z. Ao, D. Su, J. Zhang and G. Wang, *Adv. Funct. Mater.*, 2015, **25**, 1393–1403.
22 Y. X. Wang, S. L. Chou, D. Wexler, H. K. Liu and S. X. Dou, *Chem.–Eur. J.*, 2014, **20**, 9607–9612.
23 S. H. Choi, Y. N. Ko, J. K. Lee and Y. C. Kang, *Adv. Funct. Mater.*, 2015, **25**, 1780–1788.
24 G. S. Bang, K. W. Nam, J. Y. Kim, J. Shin, J. W. Choi and S. Y. Choi, *ACS Appl. Mater. Interfaces*, 2014, **6**, 7084–7089.
25 W. H. Pan, M. Leonowicz and E. I. Stiefel, *Inorg. Chem.*, 1983, **22**, 612–618.
26 P. R. Kumar, Y. H. Jung, K. K. Bharathi, C. H. Lim and D. K. Kim, *Electrochim. Acta*, 2014, **146**, 503–510.
27 H. Li, Q. Zhang, C. C. R. Yap, B. K. Tay, T. H. T. Edwin, A. Olivier and D. Baillargeat, *Adv. Funct. Mater.*, 2012, **22**, 1385–1390.
28 K. K. Liu, W. Zhang, Y. H. Lee, Y. C. Lin, M. T. Chang, C. Y. Su, C. S. Chang, H. Li, Y. Shi, H. Zhang, C. S. Lai and L. J. Li, *Nano Lett.*, 2012, **12**, 1538–1544.
29 Y. X. Wang, K. H. Seng, S. L. Chou, J. Z. Wang, Z. Guo, D. Wexler, H. K. Liu and S. X. Doua, *Chem. Commun.*, 2014, **50**, 10730–10733.
30 J. Xiao, X. Wang, X. Q. Yang, S. Xun, G. Liu, P. K. Koech, J. Liu and J. P. Lemmon, *Adv. Funct. Mater.*, 2011, **21**, 2840–2846.
31 E. A. Gulbransen, T. P. Copan and K. F. Andrew, *J. Electrochem. Soc.*, 1961, **2**, 119–123.
32 I. Kovalenko, B. Zdyrko, A. Magasinski, B. Hertzberg, Z. Milicev, R. Burtovyy, I. Luzinov and G. Yushin, *Science*, 2011, **334**, 75–79.
33 P. Ramesh Kumar and S. Mitra, *RSC Adv.*, 2013, **3**, 25058–25064.
34 L. Su, Y. Zhong and Z. Zhou, *J. Mater. Chem. A*, 2013, **1**, 15158–15166.
35 S. Hariharan, K. Saravanan, V. Ramar and P. Balaya, *Phys. Chem. Chem. Phys.*, 2013, **15**, 2945–2953.
36 S. Leroy, F. Blanchard, R. Dedryvère, H. Martinez, B. Carré, D. Lemordant and D. Gonbeau, *Surf. Interface Anal.*, 2005, **37**, 773–781.
37 D. Aurbach, A. Nimberger, B. Markovsky, E. Levi, E. Sominski and A. Gedanken, *Chem. Mater.*, 2002, **14**, 4155–4163.